# Bond Length and Charge Density Variations within Extended Arm Chair Defects in Graphene

Jamie H. Warner,[†,*] Gun-Do Lee,[‡,*] Kuang He,[†] Alex. W. Robertson,[†] Euijoon Yoon,[‡] and Angus I. Kirkland[†]

[†]Department of Materials, University of Oxford, Parks Road, Oxford OX1 3PH, United Kingdom and [‡]Department of Material Science and Engineering, Seoul National University, Seoul 151-744, Korea

ABSTRACT Extended linear arm chair defects are intentionally fabricated in suspended monolayer graphene using controlled focused electron beam irradiation. The atomic structure is accurately determined using aberration-corrected transmission electron microscopy with monochromation of the electron source to achieve ∼80 pm spatial resolution at an accelerating voltage of 80 kV. We show that the introduction of atomic vacancies in graphene disrupts the uniformity of C−C bond lengths immediately surrounding linear arm chair defects in graphene. The measured changes in C−C bond lengths are related to density functional theory (DFT) calculations of charge density variation and corresponding DFT calculated structural models. We show good correlation between the DFT predicted localized charge depletion and structural models with HRTEM measured bond elongation within the carbon tetragon structure of graphene. Further evidence of bond elongation within graphene defects is obtained from imaging a pair of 5-8-5 divacancies.
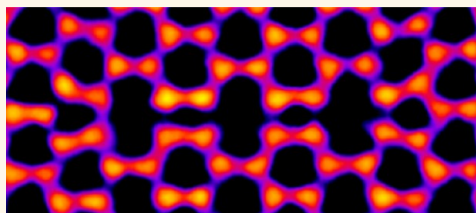
KEYWORDS: graphene · HRTEM · electron microscopy · defects · TEM

The bonding strength between carbon atoms is related to the charge density, and in simple molecules, this can be described by 'bond-order', with single, double, triple bonds, and also aromaticity arising from cyclic delocalization and resonances. Graphene sheets exhibit long-range aromaticity, equi-distribution of charge and hence uniform C−C bond lengths. A nanosized fragment of graphene can be considered as a polycyclic aromatic hydrocarbon (PAH), in which the Pauling bond order is related to the number of Kekulé resonance structures.[1−3] Since most PAH or fullerenes are small in size, there are a relatively small number of resonance structures which lead to bond length differences as recently confirmed by atomic force microscopy.[4] As the size of a PAH increases, the number of Kekulé resonance structures increases, and at the transition from PAH (nanoscale) to graphene (microscale), the number of these becomes sufficiently large that all C−C bond lengths are predicted to be identical (∼0.142 nm).[1]

However, atoms at the edge of graphene may have different C−C bond values and coordination geometries from those in the bulk due to missing nearest neighbor atoms and thus unique bonding arrangements.[5−8] The introduction of defects into a pristine graphene lattice breaks the lattice symmetry locally.[9] In particular, removal of atoms from graphene initially forms vacancies, which have been shown to subsequently undergo reconfiguration in order to maintain local bonding to three nearest neighbor atoms.[9−11] However, this process is likely to result in changes to the bonding charge distribution and to the bond lengths for C−C atoms surrounding the defect structure.

The ability to detect small deviations in C−C bond lengths surrounding defect structures in graphene requires a local imaging technique with sufficient resolution to locate the position of individual carbon atoms with suitable precision. Aberration-corrected high resolution transmission electron microscopy (AC-HRTEM) is able to resolve the lattice structure in graphene.[12−14] However, in order to accurately measure the position of atoms within graphene defects, the resolution limiting effects of damping due to partial temporal coherence at low accelerating voltages (80 kV) need to minimized. This can be achieved, either by electron optical correction of the chromatic

aberration coefficient of the objective lens or by monochromation of the electron source to reduce the energy width.[15−19]

In this report, we demonstrate that a combination of monochromated AC-HRTEM at low-voltage, multislice image simulations and density functional theory (DFT) calculations, provide insight into the mechanisms by which defects in graphene directly affect the local electronic charge distribution and bonding. To understand the relationship between the charge distribution predicted from DFT calculations and C−C bond lengths measured using AC-HRTEM, the defect structure studied must be planar, normal to the electron beam, as out-of-plane distortions skew the apparent C−C bond length in projection. Previous work has detected bond length variations around dislocation cores in graphene, but as dislocations are known to induce appreciable out-of-plane distortions this limited conclusions relating the charge to bond length.[18,20] Linear defect structures formed from the removal of atoms along the arm chair direction, rather than along the zig-zag direction that leads to dislocation pairs, are however planar. We therefore focus our present investigations on this type of defect structure. Figure 1 shows a series of schematic atomic models illustrating the missing atoms required to form an extended linear arm chair defect (LAD) that includes a four member carbon ring (tetragon). The actual step-by-step formation process of this LAD is likely to occur by the coalescence of smaller mono or divacancy defects through bond rotations.

RESULTS AND DISCUSSION

For the studies reported here, monolayer graphene was produced using chemical vapor deposition on a copper substrate and transferred onto silicon nitride TEM grids with 2 micron holes as previous reported.[21] Controlled electron beam irradiation at 80 kV was used to sputter carbon atoms from pristine regions of the as prepared graphene to create the LAD structure using conditions previously reported [9]. It should be noted that other forms of defects were also produced within the 10 nm area exposed to the focused electron beam. Figure 2 presents a comparison of DFT relaxed atomic models, multislice image simulations and strain maps calculated using geometric phase analysis (GPA).[22−24] The DFT model shows that the region of the LAD can be considered planar, while the regions to the right that contain a dislocation pair give rise to local out-of-plane distortions. The image simulation closely matches the experimental image of the LAD and the GPA shows that there is significant strain arising from bond elongation through the central region of the LAD.

A DFT calculated charge density map for the LAD structure is shown in Figures 3a,b. The vertical bonds of the carbon tetragons and terminating pentagonal rings both show appreciable charge depletion. The C−C bond lengths calculated using DFT, Figure 3c,
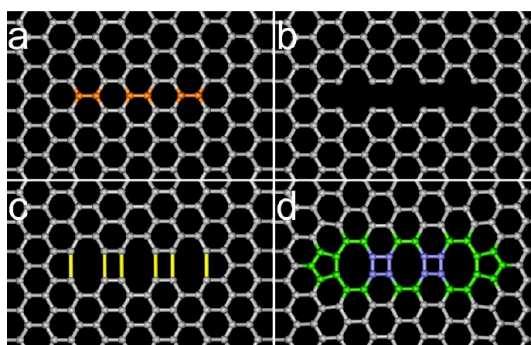

Figure 1. Schematic atomic models showing the formation of the 5-8-4-8-4-8-5 linear arm chair defect structure by atom removal. (a) Pristine graphene lattice (orange indicates atoms subsequently removed). (b) Removal of three carbon dimers (six atoms in total, orange atoms in (a)), along the arm chair direction. (c) New bonds formed (yellow). (d) After strain relaxation to form a 5-8-4-8-4-8-5 defect, with carbon tetragons shown in blue.

show clear correlation between regions of charge depletion and bond elongation, with the six vertical C−C bonds in the pentagonal rings and tetragons all elongated between 5 and 10%. Changes in bond lengths relative to a pristine region were calculated and are expressed in color on the atomic model in Figure 3c using the scale bar to the left.

To relate the bond elongations calculated using DFT to our experimental data, we have compared an image simulation of the LAD (Figure 4a) using the DFT model (Figure 3c) to the experimental HRTEM image of the LAD (Figure 4b). The C−C bond lengths shown in Figure 4a,b were determined using boxed line profile scans across two atoms to measure the distance between the maximum intensity in the peak positions, with an uncertainty of ∼5 pm (see Figure 5d). Therefore, measured bond lengths that exceed 153 pm are beyond two standard deviations and are designated as being 'above the noise' and correlate to real elongations of at least 1.07. A reference unstrained C−C bond length was measured at a distant location from the LAD structure. The strain in each bond was subsequently calculated by dividing each measured bond distance in the LAD by this reference length, (>1, elongation and <1, compression). Measurements from the image simulation (Figure 4d) and experimental image (Figure 4e) demonstrate that the bond elongation in the LAD predicted from DFT calculations can be detected from HRTEM images. Importantly, all three measurements in Figure 4c−e show that at least 5 of the 6 vertical bonds in the central region of the LAD are substantially elongated between 5 and 10%. Some of the other bonds, such as on the right-hand-side of the pentagon/octagon, also show significant elongation, which we attribute to the influence of a nearby dislocation pair that cause distortion to the lattice and is hard to accurately simulate by DFT due to the large number of atoms.
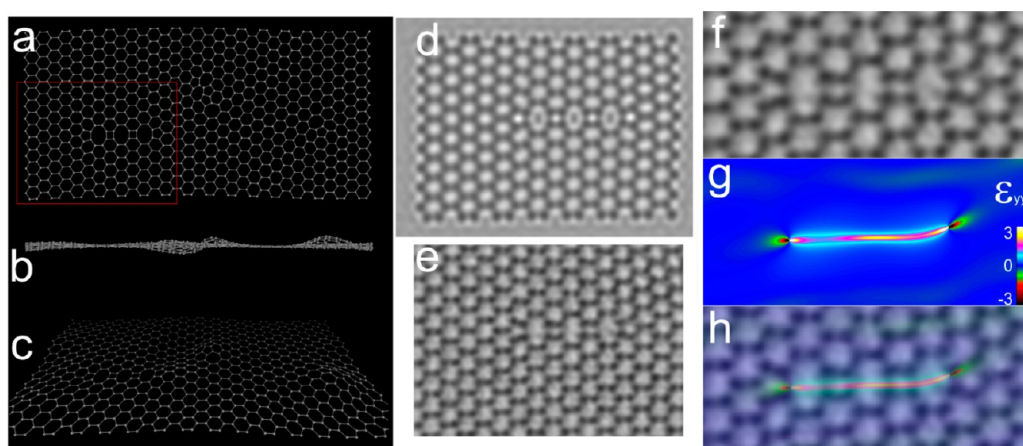
Figure 2. Comparisons of the experimental structure of a 5-8-4-8-4-8-5 linear arm chair defect (LAD) with a density functional theory (DFT) model. (a) Top view of the DFT model of defect structures observed to be produced by electron beam sputtering in graphene. (b) Side view of (a) showing out-of-plane distortions induced by dislocations, but with a relatively flat region around the tetragons in the LAD. (c) 3D perspective view showing valleys and hills in the graphene lattice from dislocations. (d) Multislice image simulation using the atomic model in (a) (red boxed region). (e) Experimental HRTEM image of a LAD created in graphene by electron beam induced sputtering. (f) Cropped region of the experimental image of the LAD structure at higher magnification. (g) Strain component (ε_{yy}) calculated using Geometric Phase Analysis (GPA) of the image in (f), color bar indicates the scale used. (h) Overlay of the GPA analysis and HRTEM image showing the relative location of the lattice strain with the atomic structure.
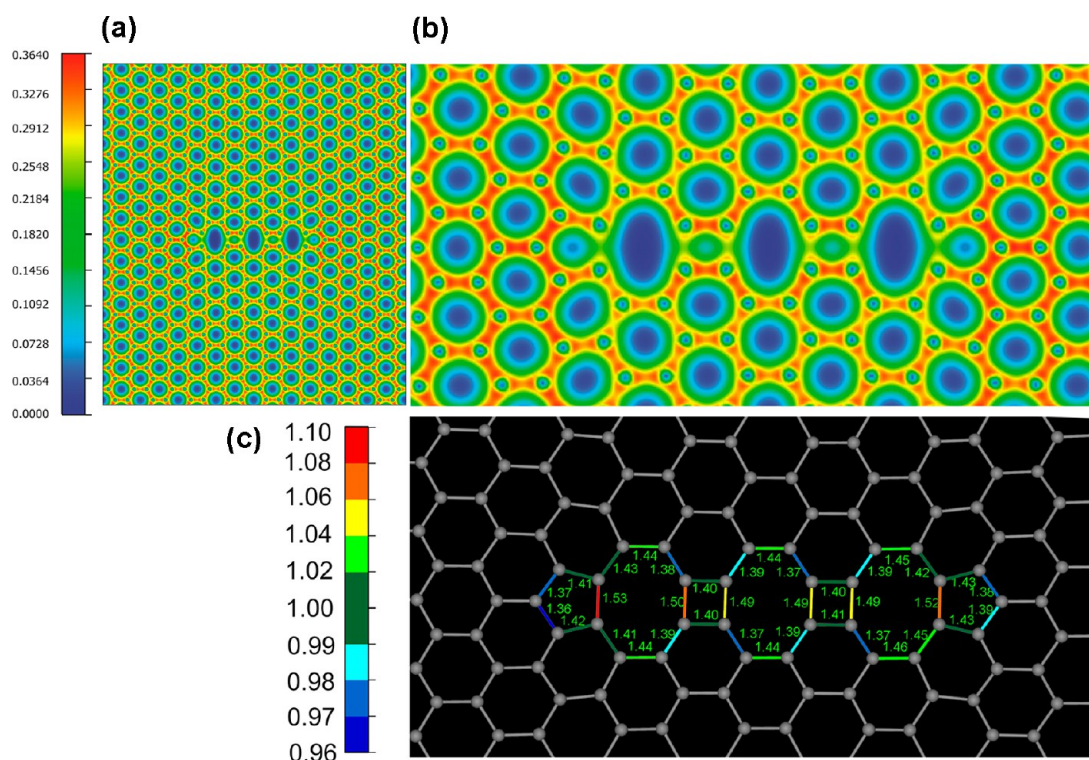
Figure 3. Correlation of charge density and bond length. (a) Total charge density determined using DFT for the atomic structure shown in Figure 2a. The unit of charge density is e/a_0^3 (a_0 is Bohr radius). (b) Higher magnification map of the total charge density for the 5-8-4-8-4-8-5 LAD structure showing charge depletion within the carbon tetragon. (c) Bond lengths in angstroms, obtained from DFT calculations for the structure in Figure 2a, focused on the 5-8-4-8-4-8-5 LAD. Error in bond length values ±0.01 Å.

The finer structural details of the carbon tetragon are compared in Figure 4f−i. These show that in the tetragon, bond elongation (measured from HRTEM images) is related to the calculated charge depletion in the vertical bond. Although the match between the all the C−C bond lengths in the DFT models, image simulations and HRTEM images is not exact, a dominant trend showing bond elongation within the central region of the LAD structure is indicated in all cases and within the experimental uncertainty of the measurements.
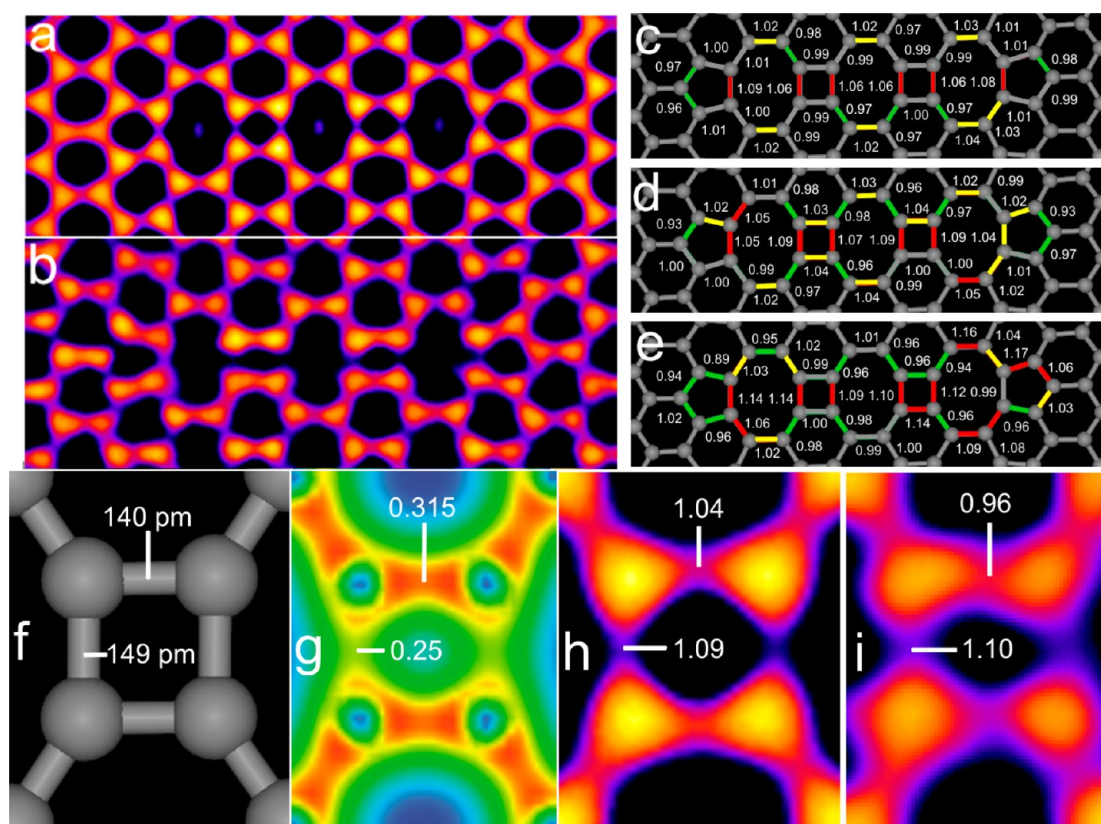
Figure 4. Charge density dependent bond length variations in carbon tetragons. (a) Multislice image simulation, as in Figure 2d, with a 'fire' color LUT for display. (b) HRTEM image, as in Figure 2e, of the 5-8-4-8-4-8-5 defect structure, with a 'fire' color LUT display. (c) Ratio of local bond length to unperturbed value, $R = B_l/B_u$, based on atomic positions from DFT calculation. (d) R value determined from the multislice image simulation in (a). (e) R value determined from the HRTEM image in (b). (f) Atomic model based on DFT calculated atomic positions for the right carbon tetragon. (g) Total charge density, as in Figure 3b of the right carbon tetragon. (h) Cropped region of (a) showing the right carbon tetragon and R values. (i) Cropped region of (b) showing the right carbon tetragon and R values.
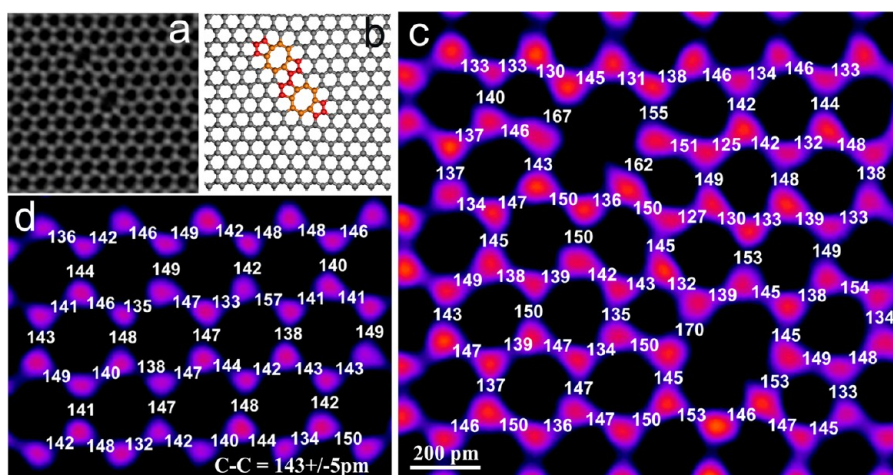

Figure 5. (a) Monochromated AC-TEM image of two 5-8-5 divacancy defects in graphene. (b) Atomic model of two 5-8-5 divacancy defects in graphene (8 atom ring = orange, 5 atom ring = red). (c) Higher magnification image of (a) with measured bond lengths in picometers. (d) AC-TEM image of a region of pristine graphene with measured bond lengths in picometers and an average C$-$C distance of 143 $\pm$ 5 pm.

Further confirmation that bond length variations exist within graphene defect structures was obtained by examining another defect composed of two neighboring 5-8-5 divacancies, as shown in Figure 5a,b. A higher magnification TEM image of the two divacancies is presented in Figure 5c and a region of pristine graphene for comparison in Figure 5d. Measurement of the distance between the centers of the contrast

spots for nearest neighbors in the pristine graphene area, Figure 5d, yields an average C–C distance of 143 ± 5 pm. In Figure 5c, all four C–C bonds at the interface between the 5–8 rings show elongated values of 167, 162, 170, and 153 pm. These values lie beyond a standard deviation and are statistically significant and represent real changes in individual C–C bond lengths. The total charge density of this defect structure was calculated by DFT and is shown in Figure 6. The four C–C bonds at the interface between the 5–8

rings that were experimentally shown to have elongated values are also the regions with the lowest charge density in Figure 6.

Figure 7 shows a comparison between the DFT predicted C–C bond lengths and those measured experimentally in Figure 5, depicted as a ratio of local bond length to unperturbed value, as in Figure 4c–e. The four major elongated bonds in Figure 7a are highlighted in pink. The experimental data also shows three of these bonds as pink, with the remaining bond partially elongated. These results confirm that C–C bonds within graphene that have lower charge density are longer and our HRTEM is capable of imaging these elongations with confidence above the noise level.
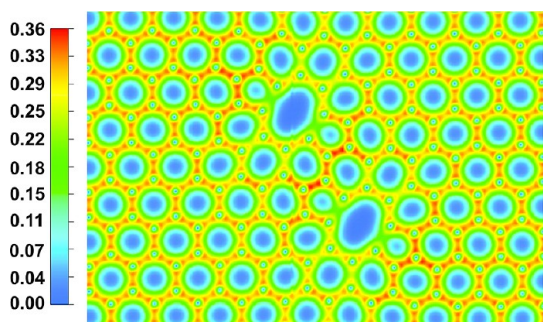

Figure 6. Total charge density of the 5-8-5 divacancy pair calculated by DFT for the atomic structure shown in Figure 5b. The unit of charge density is $e/a_0{}^3$ (a_0 is Bohr radius).

CONCLUSION

The polycrystalline continuous graphene sheets examined in this work are at least a millimeter in size, with single crystal sizes of ~100–$200\ \mu m$.[21] While we do not directly measure charge density, we have measured C–C bond lengths and compared these to DFT predicted bond lengths. The reason the predicted bond lengths by DFT are not all identical (*i.e.* 142 pm) is due to the system being comprised of purely carbon and
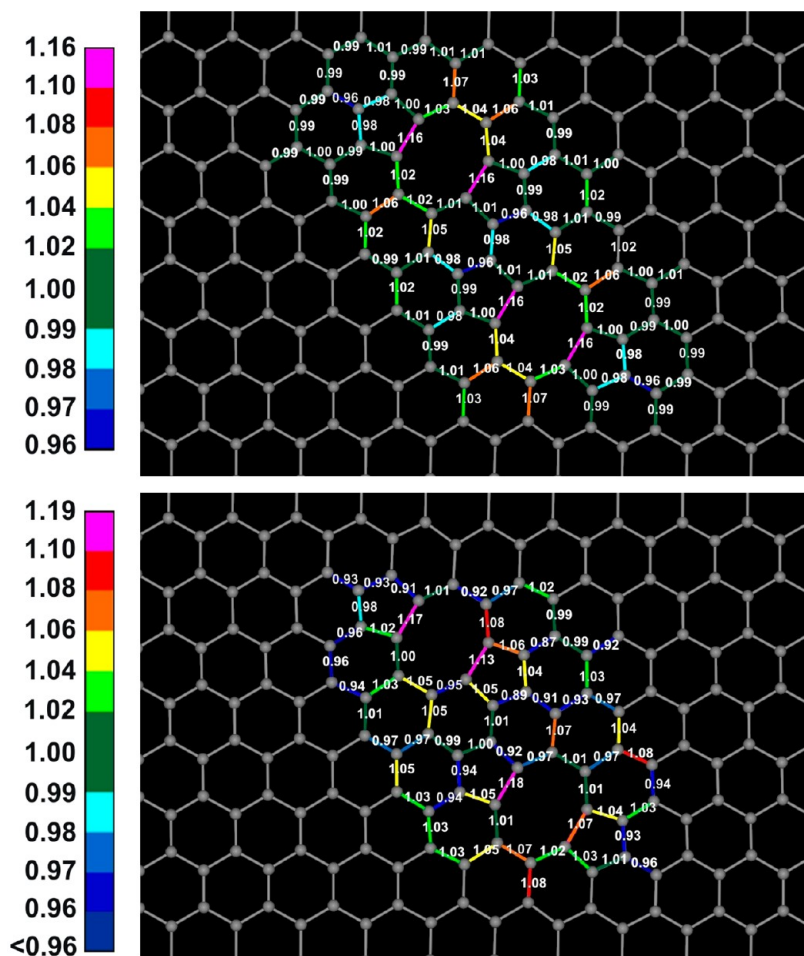

Figure 7. Ratio of local bond length relative to an unperturbed value for (top) DFT calculated structure and (bottom) experimental measurements taken from Figure 5c.

the relevant distribution of charge density between bonds. If there was no charge density variation, there would be no C—C bond length variation. Therefore, the changes we experimentally measure by HRTEM can be related to the DFT bond lengths and the DFT calculated charge density changes. The removal of atoms from a small central region leads to significant variations in the predicted bond lengths surrounding the defect formed and we have used DFT to understand how this relates to charge density changes. The planar structure of the tetragon in the LAD structure of graphene

provided an excellent platform to demonstrate the correlation between calculated charge density and experimentally measured bond lengths. An analysis of a pair of divacancies also revealed substantial bond elongation at the 5—8 ring interface region with the lowest charge density and corroborates the findings on the extended LAD structure. This is the first direct confirmation of such correlation at the single atom level in a sample that is orders of magnitude larger than small PAHs or fullerene molecules previously studied.

METHODS

Density Functional Theory Calculations. We performed density function theory calculation within the local density approximation by using a plane wave basis pseudopotential method as implemented in Vienna *ab initio* simulation package code.[25] Vanderbilt pseudopotentials are also used in this calculation.[26] The basis set contains plane waves up to an energy cutoff of 400 eV. In these electronic structure calculations, we performed two calculations. One is a calculation for a large system with 878 carbon atoms in the unit cell containing a 5-8-4-8-4-8-5 defect, a SW defect, and dislocation cores, as shown in Figure 2a. The other is a calculation for a small system with 506 carbon atoms in the unit cell containing only 5-8-4-8-4-8-5 defect to study intensively the effect of 5-8-4-8-4-8-5 defect, as shown in Figure 3a. The small system is large enough to neglect the interaction between 5-8-4-8-4-8-5 defects in neighboring unit cells.[18] Considering the missing carbon atoms from the pristine graphene structure, we contracted the graphene lattice parameter along the y-axis by 3.1% and 2.7% for the large system and small system, respectively. The unit cells also contain a vacuum region of 15 Å. Periodic boundary conditions are used in all three dimensions. The Brillouin zone was sampled using a ($1 \times 2 \times 1$) Γ-centered mesh in the large system and using ($2 \times 2 \times 1$) Γ-centered mesh in the small system. When structural relaxations are performed, the structure is relaxed until the force on each atom is smaller than 0.02 eV/Å.

Transmission Electron Microscopy. HRTEM was performed using Oxford's JEOL JEM-2200MCO field-emission gun transmission electron microscope, fitted with CEOS probe and image aberration correctors and a double Wien Filter monochromator operated with a 5 μm slit to reduce the energy spread of the electron beam to 217 meV at an accelerating voltage of 80 kV.[18] Data was recorded using a Gatan Ultrascan 4k × 4k CCD camera with 1—2 s acquisition times. The typical beam current density used for imaging was measured using a faraday cup and estimated to be $\sim$(0.2−2) × 10^6 e/(nm$^2\cdot$s). HREM image simulations were performed using JEMS software with supercells. Supercells were constructed using Accelrys Discovery Studio Visualizer.

Image Processing and Analysis. HRTEM images were processed using ImageJ. First a raw image (2k × 2k pixels) is subjected to a bandpass filter, between 100 and 1 pixels, in order to remove the long-range uneven beam illumination and then smoothed. Multiple frames (3—5) of the exact same structure are then averaged to increase signal-to-noise. A color look-up-table (LUT) of 'Fire' is used to improve visual inspection of images. The bond lengths are measured by locating the center of contrast spots in the HRTEM image and measuring the distance between them. The contrast spots associated with atoms in graphene are not exactly circular due to the hexagonal pattern, but also because the presence of defects causes deviations in the symmetry of the hexagonal lattice. These effects complicate the use of peak finding algorithms or Gaussian fits to line-profiles for accurate bond length comparisons within defects. Instead we used a combination of peak finding software with manual correction/adjustment by visual inspection for locating the best-fit for the center of the contrast spots. We have

previously shown this approach to be valid for mapping bond lengths in sp^2 hexagonal systems in ref 27.

REFERENCES AND NOTES

1. Pauling, L.; Brockway, L. O.; Beach, J. Y. The Dependence of Interatomic Distance on Single Bond-Double Bond Resonance. *J. Am. Chem. Soc.* **1935**, *57*, 2705–2709.
2. Randic, M. Aromaticity of Polycyclic Conjugated Hydrocarbons. *Chem. Rev.* **2003**, *103*, 3449–3605.
3. Sedlar, J.; Andelic, I.; Gutman, I.; Vukicevic, D.; Graovac, A. Vindicating the Pauling-Bond-Order Concept. *Chem. Phys. Lett.* **2006**, *427*, 418–420.
4. Gross, L.; Mohn, F.; Moll, N.; Schuler, B.; Criado, A.; Guitian, E.; Pena, D.; Gourdon, A.; Meyer, G. Bond-Order Discrimination by Atomic Force Microscopy. *Science* **2012**, *337*, 1326–1329.
5. Koskinen, P.; Malola, S.; Hakkinen, H. Self-Passivating Edge Reconstructions of Graphene. *Phys. Rev. Lett.* **2008**, *101*, 115502.
6. Suenaga, K.; Koshino, M. Atom-by-Atom Spectroscopy at Graphene Edge. *Nature* **2010**, *468*, 1088.
7. Koskinen, P.; Malola, S.; Hakkinen, H. Evidence for Graphene Edges Beyond Zigzag and Armchair. *Phys. Rev. B* **2009**, *80*, 073401.
8. Chuvilin, A.; Meyer, J. C.; Algara-Siller, G.; Kaiser, U. From Graphene Constrictions to Single Carbon Chains. *New J. Phys.* **2009**, *11*, 083019.
9. Robertson, A. W.; Allen, C. S.; Wu, Y. A.; He, K.; Olivier, J.; Neethling, J.; Kirkland, A. I.; Warner, J. H. Spatial Control of Defect Creation in Graphene at the Nanoscale. *Nat. Commun.* **2012**, *3*, 1144.
10. Kotakoski, J.; Krasheninnikov, A. V.; Kaiser, U.; Meyer, J. C. From Point Defects in Graphene to Two-Dimensional Amorphous Carbon. *Phys. Rev. Lett.* **2011**, *106*, 105505.
11. Banhart, F.; Kotakoski, J.; Krasheninnikov, A. V. Structural Defects in Graphene. *ACS Nano* **2011**, *5*, 26–41.
12. Meyer, J. C.; Kisielowski, C.; Erni, R.; Rossell, M. D.; Crommie, M. F.; Zettl, A. Direct Imaging of Lattice Atoms and

Topological Defects in Graphene Membranes. *Nano Lett.* **2008**, *8*, 3582–3586.

13. Hashimoto, A.; Suenaga, K.; Gloter, A.; Urita, K.; Iijima, S. Direct Evidence for Atomic Defects in Graphene Layers. *Nature* **2004**, *430*, 870–873.

14. Girit, O.; Meyer, J. C.; Erni, R.; Rossell, M. D.; Kisielowski, C.; Yang, L.; Park, C-H; Crommie, M. F.; Cohen, M. L.; Louie, S. G.; *et al.* Graphene at the Edge: Stability and Dynamics. *Science* **2009**, *323*, 1705–1708.

15. Kabius, B.; Hartel, P.; Haider, M.; Muller, H.; Uhlemann, S.; Loebau, U.; Zach, J.; Rose, H. First Application of Cc-Corrected Imaging for High-Resolution and Energy Filtered TEM. *J. Electron Microsc.* **2009**, *58*, 147–155.

16. Haider, M.; Hartel, P.; Muller, H.; Uhlemann, S.; Zach, J. Information Transfer in a TEM Corrected for Spherical and Chromatic Abberation. *Microsc. Microanal.* **2010**, *16*, 393–408.

17. Mukai, M.; Kaneyama, T.; Tomita, T.; Tsuno, K.; Terauchi, M.; Tsuda, K.; Naruse, M.; Honda, T.; Tanaka, M. Performance of a New Monochromator for a 200 kV Analytical Electron Microscope. *Microsc. Microanal.* **2005**, *11*, 2134.

18. Warner, J. H.; Margine, E. R.; Mukai, M.; Robertson, A. W.; Giustino, F.; Kirkland, A. I. Dislocation Driven Deformations in Graphene. *Science* **2012**, *337*, 209–212.

19. Warner, J. H.; Mukai, M.; Kirkland, A. I. Atomic Structure of ABC Rhombohedral Stacked Trilayer Graphene. *ACS Nano* **2012**, *6*, 5680–5686.

20. Liu, Y.; Yakobson, B. I. Cones, Pringles, and Grain Boundary Landscapes in Graphene Topology. *Nano Lett.* **2010**, *10*, 2178–2183.

21. Wu, Y. A.; Fan, Y.; Speller, S.; Creeth, G.; Sadowski, J.; He, K.; Robertson, A.; Allen, C.; Warner, J. H. Large Single Crystals of Graphene on Melted Copper Using Chemical Vapour Deposition. *ACS Nano* **2012**, *6*, 5010–5017.

22. Cowley, J. M.; Moodie, A. F. The Scattering of Electrons by Atoms and Crystals. I. A New Theoretical Approach. *Acta Crystallogr.* **1957**, *10*, 609–619.

23. Goodman, P.; Moodie, A. F. Numerical Evaluations of N-Beam Wave Functions in Electron Scattering by the Multi-Slice Method. *Acta Crystallogr., A.* **1974**, *30*, 280–290.

24. Hytch, M. J.; Snoeck, E.; Kilaas, R. Quantitative Measurement of Displacement and Strain Fields from HREM Micrographs. *Ultramicroscopy* **1998**, *74*, 131–146.

25. Kresse, G.; Furthmuller, J. Efficient Iterative Schemes for *Ab Initio* Total-Energy Calculations Using a Plane-Wave Basis Set. *Phys. Rev. B* **1996**, *54*, 11169–11186.

26. Vanderbilt, D. Soft Self-Consistent Pseudopotentials in a Generalized Eigenvalue Formalism. *Phys. Rev. B* **1990**, *41*, 7892–7895.

27. Warner, J. H.; Young, N. P.; Kirkland, A. I.; Briggs, G. A. D. Resolving Strain in Carbon Nanotubes at the Atomic Level. *Nat. Mater.* **2011**, *10*, 958–962.